.

L0 constrained sparse reconstruction for multi-slice Helical CT reconstruction

Yining HU[1,3], Lizhe XIE[1,3], Limin LUO[1,3], Jean Claude NUNES[2,3] and Christine TOUMOULIN[2,3]

[1]Laboratory of Image Science and Technology (LIST), South East University, 210096 Nanjing, China
[2]Laboratoire Traitement du Signal et de l'Image (LTSI) INSERM U642, Université de Rennes I, Campus de Beaulieu, 263 Avenue du Général Leclerc - CS 74205 - 35042 Rennes Cedex
[3]Centre de Recherche en Information Biomedicale Sino-Francais (LIA CRIBs), Rennes, F-35000, France

E-mail: caiest@hotmail.com,christine.toumoulin@univ-rennes1.fr

Abstract. In this paper, we present a Bayesian maximum a posteriori (MAP) method for multi-slice helical CT reconstruction based on a L0-norm prior. It makes use of a very low number of projections. A set of surrogate potential functions is used to successively approximate the L0-norm function while generating the prior and to accelerate the convergence speed. Simulation results show that the proposed method provides high quality reconstructions with highly sparse sampled noise free projections. In presence of noise, the reconstruction quality is still significantly better than the reconstructions obtained with L1-norm or L2-norm priors.

1. Introduction

In recent years, multi-slice helical computed tomographic devices have become world-wide marketed. They offer high spatial and temporal resolutions capable for instance to image the beating heart in 3D and to provide access to small structures like the coronary arteries and veins (Ropers et al.; 2003; Becker et al.; 2002; Nieman et al.; 2001). In spite of the remarkable advantages of multi-slice helical CT, the X-ray dose exposure remains a major concern in clinical practice (Rogers; 2002; Slovis; 2002; Rusinek et al.; 1998; Naidich et al.; 1990; Pouliot et al.; 2005). Irradiation can be decreased by reducing the X-ray intensity. However this inevitably degrades the signal to noise ratio in measurements and subsequently the reconstructed image quality (Hsieh; 1997; JUNG et al.; 2000). Several sinogram smoothing approaches have been proposed to reduce the noise (Li et al.; 2004; La Rivière; 2005; Wang et al.; 2006). In the present study, instead of lowering X-ray intensity, we address this problem by limiting the number of scan projections. Statistical image reconstruction, although requiring high storage capacity and large computation resources, is a sound way to deal with such situation. These iterative methods have been widely exploited for tomographic reconstruction and are today well established (Manglos et al.; 1995; Knaup et al.; 2006; Thibault et al.; 2003; Nielsen et al.; 2005; Sukovic and Clinthorne; 2000; Iatrou et al.; 2006). They allow introducing constraints such as non-negativity,

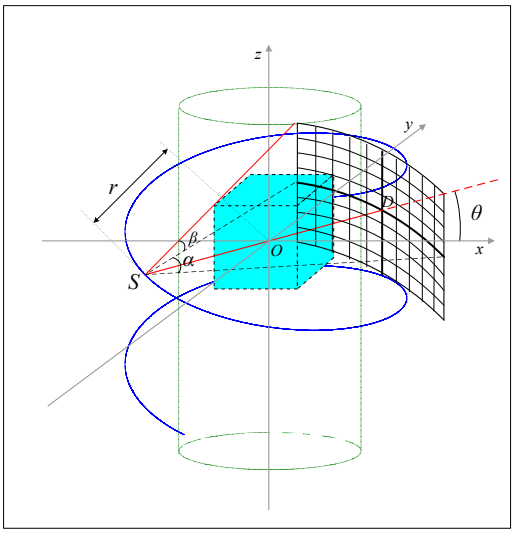

Figure 1. Scanning configuration.

image bounds, object sparsity, etc. The approach reported for instance by Sidky and Pan for circular cone-beam configuration (Sidky and Pan; 2008) shows that limited angle and under-sampled projections can be dealt with. It combines Projection Onto Convex Set (POCS) search and total variation (TV) prior.

Our objective here is to point out that a L0-norm prior with a MAP model (section 2) can offer a suitable solution for sparse projection systems. In section 3, we describe the optimization method based on the separable paraboloidal surrogates (SPS) algorithm used for improving the convergence speed (Fessler and Erdogan; 1998). The performance of the proposed method, L0-SPS, is evaluated in section 4 on the 3D Shepp-Logan phantom, with and without noise and by varying the number of projections per rotation from 8 to 24. The results are then discussed in section 5 before concluding.

2. Theory

2.1. Image Model

The scanning configuration is shown in Fig. 1 where the helical trajectory is depicted in blue. For practical reasons, the X-ray source and detector plane follow a circular trajectory while the bed (i.e the patient) is simultaneously translated along the rotation axis, with the rotation and translation speeds being constant. S is the x-ray source and O is the center of rotation axis. $\overrightarrow{SD}$ is perpendicular to the detector plane (i.e., the z-axis). $|\overrightarrow{SO}| = r$ indicates the distance between the x-ray source and the rotation axis. With a fixed-coordinate system, the trajectory of X-ray source can be expressed as:

$$S(\theta) = (r\cos(\theta), r\sin(\theta), h\frac{\theta}{2\pi}) \tag{1}$$

where θ denotes the rotation angle of the x-ray source, and h is the pitch.

Although (1) is continues, in real CT scans, both image function and measurements are sampled. If the sampling count for the rotation angle θ is L, we have:

$$\theta \in \{\theta_1, \theta_2, \cdots, \theta_L\} \tag{2}$$

and consequently, the source positions are described by:

$$S \in \{S(\theta_1), S(\theta_2), \cdots, S(\theta_L)\} \tag{3}$$

Suppose there are B(rows)$\times C$(columns) detectors evenly placed on detector plane, then, when $S = S_l$, the coordinate of detector center at row b column c is $D_{l,b,c}$ and the ideal measurements are given by a set of line integrals through the continuous function:

$$g(\theta_l, b, c) = \int_0^{+\infty} f\left(S_l + t\,\overrightarrow{u}_{l,b,c}\right) dt \tag{4}$$

where $\overrightarrow{u}_{l,b,c}$ is the unit vector in the direction of $\overrightarrow{S_l D_{l,b,c}}$, f is the unknown 3D object density function to be reconstructed. This integral, when discretized, can be expressed in matrix form:

$$\boldsymbol{g} = \boldsymbol{A}\boldsymbol{f} \tag{5}$$

with f, the image vector, and g, the projections Matrix $\boldsymbol{A}$ is the numerical approximation of the line integrals depicted in (4), named as system matrix or projection matrix. By setting J, the number of voxels in the volume image and I, the number of measured projections, the cardinals of vectors g and f are $1 \times J$ and $I \times 1$ respectively, the size of A being $I \times J$ In most cases A is a highly sparse matrix. However besides the projection geometry, other factors when modeling the system matrix must be taken into consideration such as the attenuation, the detector efficiency, etc.

2.2. MAP model

Having generated the system matrix, we now focus on the optimization model of the reconstruction problem. According to Bayesian theory, a MAP estimator of image vector $\boldsymbol{f}$ is defined as:

$$\widehat{\boldsymbol{f}}(\boldsymbol{y}) = \arg\max_{\boldsymbol{f}} \{L(\boldsymbol{y}|\boldsymbol{f}) - \beta R(\boldsymbol{f})\} \tag{6}$$

The objective function is composed of two terms. $L(\boldsymbol{y}|\boldsymbol{f})$, the log-likelihood function, reflects the statistical features of the projection data. In CT scanners, the projection data are usually degraded by many factors, such as background noise, random noise, scatter effect and so on. Thus, a pre-correction should be required before reconstruction. All these factors above make the statistical features complicated. It is suggested in (Lu et al.; 2001) that noise property of the projection data for low-dose CT scan can be assumed as normally distributed with a nonlinear signal-dependent variance. The elements in the measurement vector are supposed to follow independent Gaussian distributions with mean value the ideal line integrals along the X-rays:

$$y_i = \frac{1}{\sqrt{2\pi\sigma_i}} exp\left\{-\frac{(y_i - g_i)^2}{2\sigma_i^2}\right\} \tag{7}$$

where σ_i is the variance.

The corresponding log-likelihood function is:

$$L(\boldsymbol{y}|\boldsymbol{f}) = \sum_{i=1}^{I} -\frac{1}{2}\{(\boldsymbol{y}-\boldsymbol{A}\boldsymbol{f})'\boldsymbol{\Sigma}^{-1}(\boldsymbol{y}-\boldsymbol{A}\boldsymbol{f}) - \ln(2\pi\boldsymbol{\Sigma})\} \tag{8}$$

where $\boldsymbol{\Sigma}$ is the covariance matrix. Since the projections are supposed to be independent, $\boldsymbol{\Sigma}$ is diagonal and $\boldsymbol{\Sigma} = diag\{\sigma_i\}$

The second term in (6) is the image prior, which acts as a penalty term in the MAP model, and β is a positive hyperparameter, which controls the weight of the image prior. We here consider penalties that can be expressed in the following very general form:

$$R(\boldsymbol{f}) = \sum_{j}\sum_{k\in N_j} \omega_{kj}\psi(\boldsymbol{f}_j - \boldsymbol{f}_k) \tag{9}$$

where N_j is the neighborhood region of jth voxel, ω_{kj} is a positive value that denotes the interaction degree in clique kj. Usually, it is inversely proportional to the distance between pixel pairs. $\psi(t)$ is potential function.

The TV prior applied by Sidky and Pan (Sidky and Pan; 2008) to the reconstruction is similar to the L1-norm prior with a potential function, $\psi(t) = |t|$. Although Donoho (Donoho; 2006) have proven the L0 semi norm prior is equivilent to L1 norm prior in signal recovery in some linear systems, yet this is no longer true when the sampling rate of measurements is too low (Candès and Romberg; 2005). In our approach, we choose L0-norm prior for the reconstructionand and the potential function is then defined as:

$$\psi(t) = |sgn(t)| \tag{10}$$

L0-norm is not continuous and numerical difficulties exist when trying to solve (6) directly. Chartrand proved that by replacing the L1-norm with the Lp-norm with $p < 1$, exact reconstruction of sparse signal is possible with substantially fewer measurements (Chartrand; 2007). Therefore, by choosing a p small enough, the L0-norm may be approximated by Lp-norm. More generally, any function satisfying

$$\lim_{\rho\to 0}\psi(t,\rho) = |Sgn(t)| \tag{11}$$

can be taken as potential function.

Yet, another problem has to be addressed. The L1-norm prior is proven to be closely related to the total variation prior (they are equivalent in 1D case). This brings us a convex optimization problem that can be solved efficiently. However the Lp-norm ($0 < p < 1$) prior is non-convex. When choosing a relatively small p, the optimization to (6) may not reach the global minima. Candès have introduced a reweighted L1 minimization scheme for compressive sampling (Candès et al.; 2007). In his work, a convave (not convex) objective function, which is more closely resembles the L0 norm was considered. His work can be taken as a special case of the method Trzasko (Trzasko and Manduca; 2009) introduced. In Trzasko's work, an asymptotic optimization scheme for the L0-minimization by approximating the L0-norm with a set of non-convex potential functions. The following potential function is used in our approach:

$$\psi_{L_0}(t,\rho) = \log\left(\frac{|t|}{\rho} + 1\right) \tag{12}$$

Other surrogate functions could be considered such as:

$$\psi_{L_0}(t,\rho) = (1 - exp\,(-|t|/\rho)) \tag{13}$$

or

$$\psi(t,\rho) = \frac{2}{\pi}\arctan\left(\frac{|t|}{\rho}\right) \tag{14}$$

Although with a smaller ρ, the semi-L0-norm better approximates the "true L0-norm" defined in (10), it has been proven that to ensure the convergence to the global optimum, the initial guess should be close enough to the solution. Otherwise the algorithm will more likely find a local minimum of the objective function, leading then to highly distorted reconstructions. In order to avoid this situation, a progressive scheme is applied in this paper. The optimization starts with a relatively large ρ (hence the initial guess does not have to be close to the final reconstruction), then ρ is reduced when the optimization converges. By successively reducing the value of ρ, the optimization gradually approaches the expected result.

3. Optimization

3.1. Quadratic Form Objective Function

Various algorithms have been proposed for the optimization of (6). Fessler (Fessler and Erdogan; 1998; Erdogan and Fessler; 1999b,a) introduced separable paraboloidal surrogates (SPS) algorithm for tomographic reconstruction, originally designed for Poisson statistics. It should be noticed that the optimization of quadratic objective functions is easier than non-quadratic forms. The SPS algorithm is based on paraboloidal surrogate functions for the log-likelihood which transform the problem into a simple quadratic optimization. This idea has been retained here due to the significant performance achieved in accelerating the convergence speed.

Given projection model and system matrix $\boldsymbol{A}$, the log-likelihood function can be taken as function of ideal projection vector $\boldsymbol{g}$:

$$L(\boldsymbol{g}) = \sum_{i=1}^{I} L_i(g_i) = \sum_{i=1}^{I}\left(\frac{(y_i - g_i)^2}{2\sigma_i^2}\right) \tag{15}$$

Substituting (5) into (15), the log-likelihood is then:

$$\widetilde{L}_j(f_j;\widehat{\boldsymbol{f}}) = \sum_i L_i(g_i;\widehat{\boldsymbol{g}}) = \sum_i L_i((\boldsymbol{A}\boldsymbol{f})_i;\boldsymbol{A}\widehat{\boldsymbol{f}}) \tag{16}$$

According to Taylor expansion, the voxel-based quadratic log-likelihood function should have the following form:

$$\begin{aligned} Q_j(f_j) = \widetilde{L}_j(\widehat{\boldsymbol{f}}) &+ \frac{\partial}{\partial f_j}\widetilde{L}_j(\widehat{\boldsymbol{f}})|_{f_j=\widehat{f}_j}(f_j - \widehat{f}_j) \\ &- \frac{1}{2}d_j(f_j - \widehat{f}_j)^2 \end{aligned} \tag{17}$$

and

$$Q(\boldsymbol{f}) = \sum_j Q_j(f_j) \tag{18}$$

with

$$\dot{L}_j(f_j) = \frac{\partial}{\partial f_j}\widetilde{L}_j(\widehat{\boldsymbol{f}}) = \sum_i \frac{\partial L_i}{\partial g_i}\frac{\partial g_i}{\partial f_j}$$

$$= \sum_i a_{ij} \frac{\partial L_i}{\partial g_i}$$
$$= \sum_i a_{ij} \dot{L}_i(\widehat{g}_i) \tag{19}$$

According to (15),

$$d_j = \sum_i a_{ij}^2 \ddot{L}(g_i) = \sum_i a_{ij}^2 \sigma_i^2 \tag{20}$$

for the penalty part, a quadratic form surrogate function is also needed. In Erdogan and Fessler's work (Erdogan and Fessler; 1999b,a), only convex priors are considered. According to their method, it is usually difficult to get a quadratic surrogate directly for non-convex priors. Hence, we simply separate the update into 2 steps:

$$f_j^{k+1,1} = f_j^k + \frac{\dot{L}_j(f_j)}{d_j} \tag{21}$$

then

$$f_j^{k+1,2} = f_j^{k+1,1} + \beta \frac{\partial R(\boldsymbol{f})}{\partial f_j} \tag{22}$$

and considering the non-negative constraints, we have:

$$f_j^{k+1} = max(\tilde{f_j}^{k+1,2}, 0) \tag{23}$$

3.2. Algorithm

From (21), we may see that the update of each voxel f_j requires the computation of $\dot{L}_j(f_j)$, and d_j. For a 3D volume reconstruction, the number of voxels is quite large and, although the update of $\dot{L}_j(f_j)$ accelerates the convergence, it takes too much time for a single iteration. To balance the convergence and computation speed, we followed Fessler's idea of space-alternating updates in parameters (Fessler and Hero; 1994, 1995). We separate the voxel set into several disjoint subsets $\boldsymbol{f}^{(t)}$ satisfying:

$$\boldsymbol{f}^{(t)} \subset \boldsymbol{f}, t = 1, \cdots, T; \bigcup_{i=1}^{T} \boldsymbol{f}^{(i)} = \boldsymbol{f}; \tag{24}$$

the updates for $\dot{L}_j(f_j)$ and d_j are only performed after all voxels in one subset is updated. In this paper, the 3D object is divided into several horizontal slices, each being taken as a subset. Yet, we must notice that in the SPS algorithm with Poisson statistics, the computation cost of d_j is quite high since it is the sum of curvatures of the surrogates function, that has to be recomputed one by one (pre-computation of curvatures has been suggested to face this problem (Erdogan and Fessler; 1999b,a)). The advantage with Gaussian statistics is that the curvatures $\ddot{L}(g_i)$ are always 1.

The whole algorithm is illustrated as follows:

- Initialize: set $\boldsymbol{f}^0$.
- Set parameters β^0 and ρ^0
- calculate d_j using (20);
- Outer iteration: for $n = 1, \cdots$, N
  - Inner iteration:

  - ∗ calculate $\boldsymbol{g}$ according to (5);
  - ∗ For $t = 1, \cdots, T$:
    - · calculate $\dot{L}(f_j)$ according to (19) for each $f_j \in \boldsymbol{f}^{(t)}$;
    - · update $\boldsymbol{f}^{(t)}$ using (21) and (22) ;
    - · update g_i using (5);
  - ∗ check stopping condition, continue inner iteration if condition not reached;
- set $\beta^{n+1} = u_\beta \beta^n$, $\rho^{n+1} = u_\rho \rho^n$;

u_β is a relaxation parameters satisfying $0 < u_\beta < 1$ and so is u_σ. For the initialization, we can simply set $\boldsymbol{f}^0$ to a constant or make use of a filtered backprojection reconstruction (FBP) (Zou and Pan; 2004) with sparse projections which will need fewer iteration to get convergence (in our approach, FBP were chosen for initialization, fewer iterations are needed but the initialization does not affect on the final result). For the inner iteration, a commonly used stopping criterion is:

$$|\boldsymbol{f}^{n,m+1} - \boldsymbol{f}^{n,m}| < \epsilon \tag{25}$$

where n and m are outer and inner iteration number, ϵ is small positive constant. In our approach, we have to set different ϵ for each outer iteration because the objective function is changed. Instead of introduce a variable ϵ, we can use the following stopping rule:

$$|\boldsymbol{f}^{n,m+1} - \boldsymbol{f}^{n,m}| < \epsilon |\boldsymbol{f}^{n,2} - \boldsymbol{f}^{n,1}| \quad or \quad m \leq M \tag{26}$$

Here M is an empirical limit of the inner iteration number, to prevent the algorithm from falling into an infinite loop when dealing with improper parameters or poor quality projections. The inner iteration number depends largely on the tolerance ϵ. By reducing ϵ, the inner iteration number generally increases (no more than M) and a better convergence is likely to obtain for each outer iteration. However, there's no need to set a very small value for ϵ to obtain a very high degree of convergence, because a quick descent stage for the reconstruction error already occurs once the algorithm runs into a new outer iteration.

4. Experiments

Experiments have been realized on a 3-D Shepp-Logan phantom, modified to include highly contrasted objects nearby low contrast structures so as to consider a more realistic model of anatomical variations. We performed two sets of simulations. The first one was designed to validate the efficiency of the L0-SPS method. Noiseless measurements were generated by means of the modified 3D Shepp-Logan phantom knowing the system matrix. Three orthogonal slices through the 3-D modified phantom are seen in Fig. 2. The detector dependent factors (such as detector efficiency coefficients) were set to 1. The second simulation was then conducted with noisy data. We also used the modified 3D Shepp-Logan phantom, but the model was made more realistic by adding Gaussian noise to the ideal measurements to simulate the real scan. In these two simulations, the system configuration was the same. The 3D volume was set to $200 \times 200 \times 200$ voxels. The size of each voxel was $2.0mm \times 2.0mm \times 2.0mm$. The source to iso-center distance was 700mm and the source to detector distance was 1400mm. We considered 16 detector rings, each of which covers a fan angle of 75^o with 256 detectors. For each cycle, the source rotates over 360^o, the source trajectory was covered by 16 view angles and the pitch is set to 12. The whole scan runs 4 cycles.

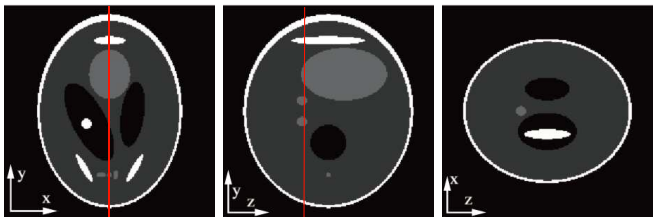

(a) (b) (c)

Figure 2. Visualization of three slices at respectively (a) z = 0 mm, (b) x = 0 mm, (c) y = -20 mm through the 3-D modified Shepp-Logan phantom: several high and low contrast structures have been added that are of different sizes and close to each other to evaluate the performance of the algorithm on a more realistic anatomical model. Three kinds of structures are highlighted by an arrow and a vertical line has been drawn in slice (a) and (b) respectively, along which intensity profiles will be further displayed.

The number of measured rays was 262144. All computations in the simulation were performed on a PC (Intel processor, 2.8-GHz CPU and 4GB RAM) using Microsoft visual C++ 2008.

We compared in the following 3 priors: L2-norm, L1-norm and the proposed L0-norm prior. Note that the potential function for L1-norm prior is not differentiable at zero, thus we used the following smooth approximation:

$$\psi_{L1}(t) = \sqrt{f^2 + \kappa} - \sqrt{\kappa} \tag{27}$$

where κ is a small positive constant(set to be 10^{-5}).

4.1. Simulation Results

We first applied the proposed method to the reconstruction of noise free projection data. For L0-norm prior, the initial parameters were: $\beta^0 = 1.0, \rho^0 = 2.0$, relaxation parameters $u_{beta} = 0.5$, $u_\rho = 0.5$, outside iteration number $N = 10$ and for inner iteration, $\epsilon = 0.2$ and $M = 120$. For L1 norm and L2 norm prior, iteration numbers were set to 1000. We performed a set of experiments with different parameters and computed the root mean square error (RMSE) between the reconstructed phantom and its ground truth. We selected as optimal parameters, the one which brought a compromise between the minimization of the RMSE and the variance on different regions. We found thus $\beta = 0.2$ for L1 norm prior and $\beta = 3.0$ for L2 norm prior. The visual inspection of the reconstructed phantom (Fig. 3) shows that the reconstructions with L0-norm prior match well with the origin phantom images, whereas the distortion in the results with L1-norm and L2-norm prior are comparatively high. Fig.4 presents a density profile corresponding to the vertical lines (in red) placed in Fig. 2 (a) and (b), which also confirm that with L0-norm prior, the reconstruction quality is better than with the 2 other priors.

We made then vary the number of projections from 8 to 24 per cycle and performed the reconstruction using the L0-norm prior. Results displayed in Fig. 5, show that small objects are not well reconstructed with 8 projections per cycle, whereas with 24 projections, the result looks better. The reconstruction quality improves with the increasing of projection number. This is confirmed by the RMSE ratio computed

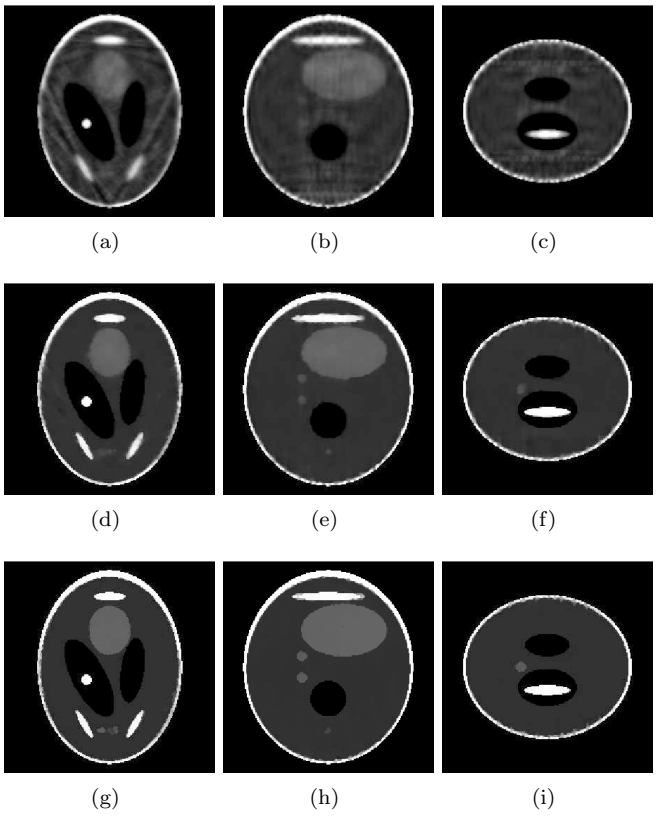

(a) (b) (c)

(d) (e) (f)

(g) (h) (i)

Figure 3. Reconstruction results with noise free projections. From top to bottom are with L2, L1 and L0-norm priors. From left to right: 2D slices at z = 0 mm, x = 0 mm, and y = -20.0 mm. The RMSE ratios are 10.19%, 8.53%, and 3.95% for L2, L1 and L0 norm priors respectively.

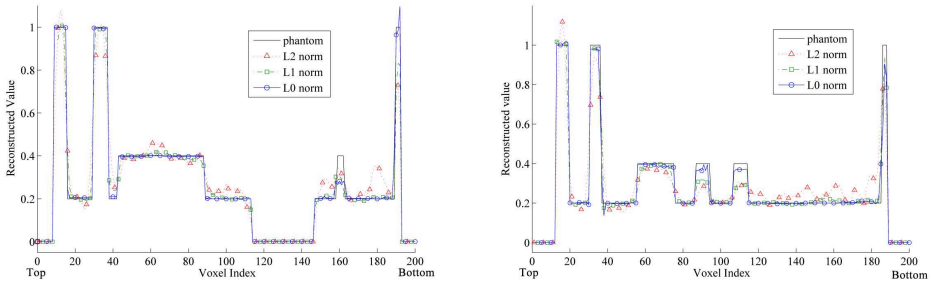

(a) (b)

Figure 4. Intensity profile along the vertical lines placed in Fig 2.a (100th column, z = 0 mm) and 2.b (78th column, x = 0 mm). The black solid line corresponds to the ground truth, the dash lines with triangle, square and circle markers represent the L2 norm, L1 norm and L0 norm respectively.

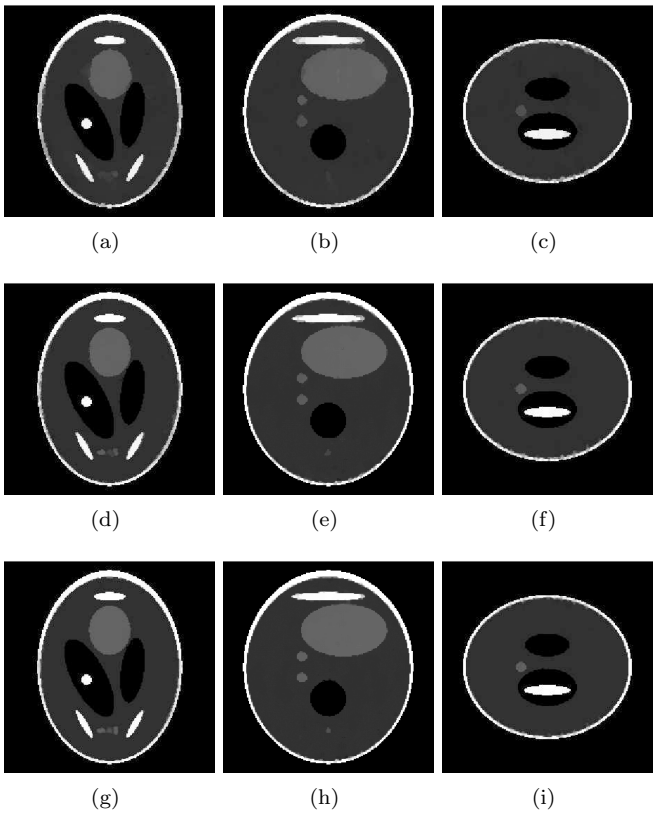

Figure 5. Reconstruction with L0-norm prior and with different number of views and noise free projections. From top to bottom, results with 8, 16, 24 projections per cycle. The RMSE ratios are 5.74%, 3.95%, and 2.58% for 8, 16, 24 projections per cycle, respectively.

for each reconstruction. However, both the projection matrix size and the computational time increase with the number of projection views.

The simulations above have been carried out by considering a discrete to discrete imaging model. Nevertheless, a real imaging system is a continuous to discrete transform. The voxelization may bring some effect especially at the frontier of regions. To better evaluate such effect, we added a small high contrast region in the phantom, generated then the projections using discrete and continuous imaging model respectively. We performed the reconstruction with the L0 norm prior using the same parameters as before. Fig.6 shows the reconstruction results for each imaging model i.e. discrete to discrete and continuous to discrete respectively. The object appears smooth in the first case with slightly fuzzy edges. These latter are better preserved in the second case to the detriment however of the appearance of a strong texture inside the regions (Fig. 6-j). This result could be improved with a higher resolution of the object (currently $2 \times 2 \times 2mm^3$). Nevertheless a compromise must be struck between improving the quality and obtaining a reasonable computational time. Multiresolution reconstruction could be an effective way to solve this problem by introducing

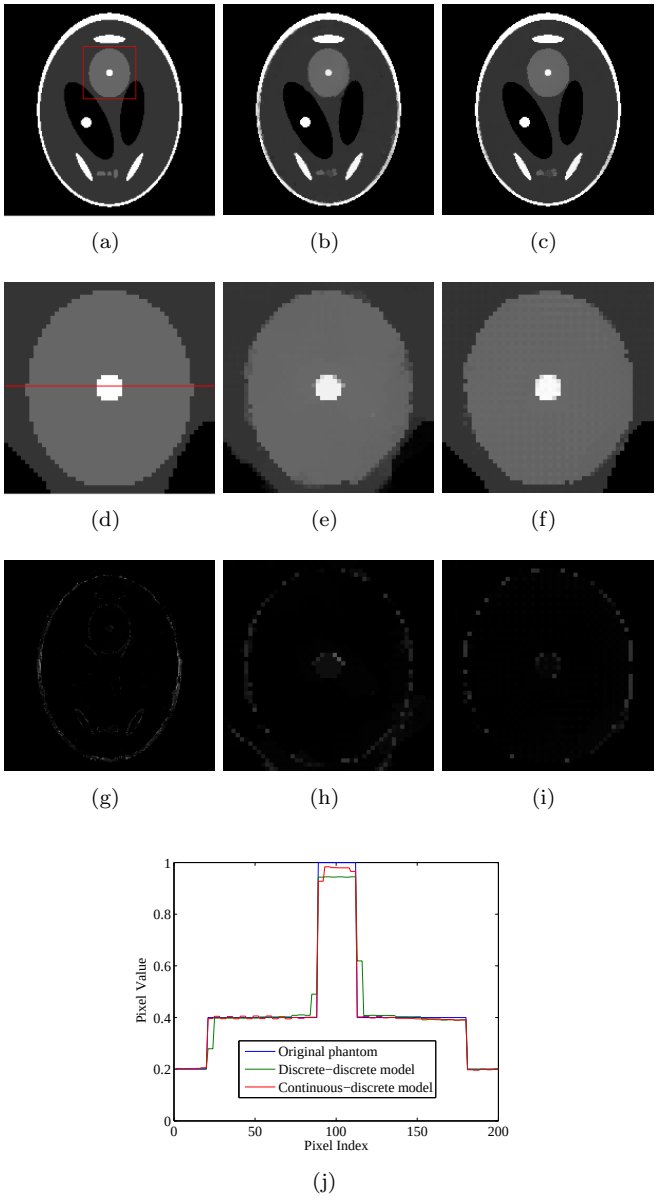

Figure 6. Comparison of different imaging models. (a): original phantom at slice $z = 0$, the ROI is delimited with a red box; (b): reconstruction result from a discrete to discrete imaging model, at slice $z = 0$, RMSE 4.08%; (c): reconstruction result from a continuous to discrete imaging model, at slice $z = 0$, RMSE 3.25%; (d)(e)(f): visualization of the ROI displaying the original data (from (a)) and after reconstruction (from (b) and (c)); (g)(h)(i) provide the difference between (b) and (c), (b) and (a), (c) and (a) respectively; (j) Normalized intensity profiles along the red horizontal line drawn in (d), (e) and (f)

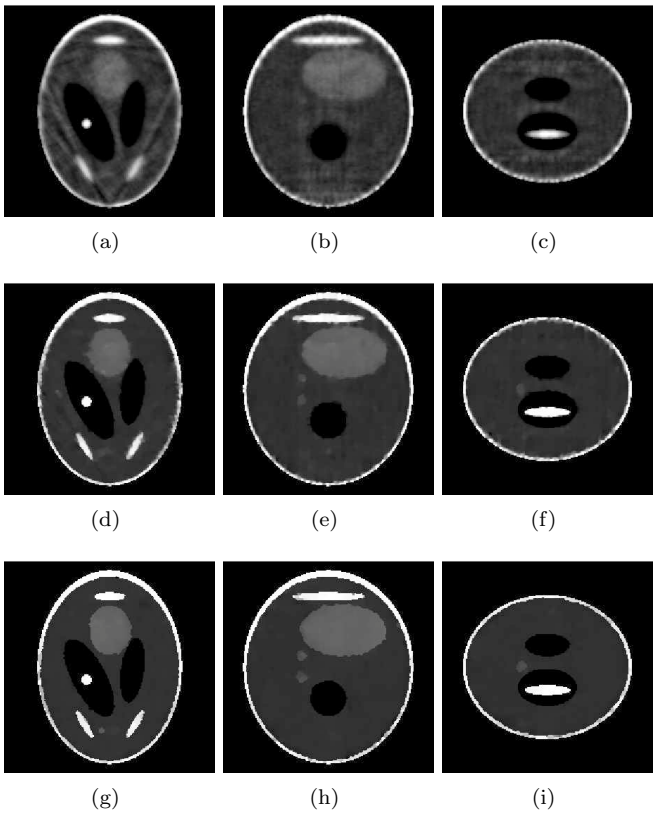

Figure 7. Reconstruction results with noisy projections (0.5% additive Gaussian noise). The top to bottom and left to right rules are identical to those depicted figure 3. The RMSE ratios are 12.12%, 9.75%, and 5.91% for L2, L1 and L0 norm priors respectively.

a high resolution in some specific ROIs and normal or less resolution in other parts of the object. This will be a further direction of our work.

We evaluated then the behavior of these methods in presence of noisy measurements for 16 angles of views per cycle. A 0.5% Gaussian noise was added to the projection data. For the L0-norm reconstruction, the parameters were set as follows: $\beta^0 = 1.0, \rho^0 = 2.0, u_\beta = u_\rho = 0.65$. For L1-norm and L2-norm, the hyperparameters were computed as previously to find a compromise between the minimization of the RMSE and the variance in large regions. These parameters were $\beta = 0.3$ and $\beta = 4.0$ respectively. Reconstruction results shown in Fig. 7 indicates that L0 norm prior also provides the best results with a RMSE equal to 5.91%. Although the L1-norm prior method has a better performance than the L2-norm prior in providing smoother reconstructions, details of the phantom can hardly be recognized in the reconstructions. The reason is that L1-norm prior needs more number of projections to provide a satisfying quality. Fig. 8 presents the density profile corresponding to the vertical lines in Fig. 2 (a) and (b). It shows that the L0-norm better preserves the transitions and the constant values.

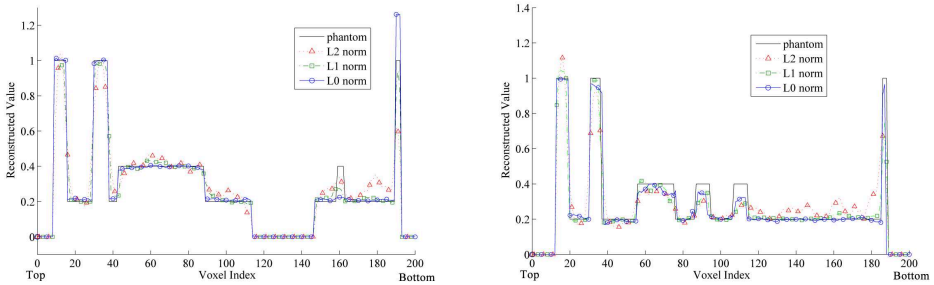

Figure 8. line profile for noisy projections (0.5% additive Gaussian noise) reconstructions, corresponding to vertical line placed in Fig. 2 (a) and (b)

We then increased the Gaussian noise level to 2%. For the L0-norm reconstruction, the parameters are set as follows: $\beta^0 = 2.0, \rho^0 = 2.0, u_\beta = u_\rho = 0.7$. For L1-norm and L2-norm, the optimal hyperparameters were found to be $\beta = 0.4$ and $\beta = 5.0$ respectively. The reconstructed slices are shown in Fig. 9, and Fig.10 is the corresponding intensity profiles along the vertical lines set in Fig. 2. Although L0-norm provides better results than L1 and L2 priors in the reconstruction of the modified phantom, we see that when the noise increases, small structures are not well reconstructed and edges turn out to be blurred. The hyperparameters were chosen to produce the best RMSE ratio.

4.2. Parameters

As mentioned in section 3.2, the parameter ρ was iteratively decreased to better approximate the "true L0-norm prior". For this purpose, we have used a relaxation parameter u_ρ to dynamically modify ρ. As the L0-norm is non-convex, the algorithm could fall into local minima if u_ρ is not properly chosen. Such effect often appears as bright spots in the reconstructions. In the experiments above u_ρ was set to 0.5 for noise free projections and 0.65 for noisy projections. u_ρ was made vary for reconstructing the volume from noisy projections (0.5% Gaussian noise added). Results are shown in Fig. 11 and Fig. 12 for the corresponding RMSE plots. They pointed out that as the value of u_ρ increases, the reconstruction quality is first improving and then degrading.

5. Discussion

The advantages of the L0-SPS method over the L1 and L2 norm priors have been highlighted above for sparse projections, in noise and noise-free situations. Nevertheless, some problems are still to be faced.

First of all, the time computation is high. For example, with 4 cycles, 16 angles per cycle, each elementary iteration takes about 30 seconds at first, and reduced to about 8 seconds after rearranging the subsets. There are several other ways to reduce the computing workload. It can be done by separating the 3D image into more subsets: although the time required for each iteration is increased, fewer iterations are needed to get convergence, therefore the total time cost is reduced. Parallel computing can

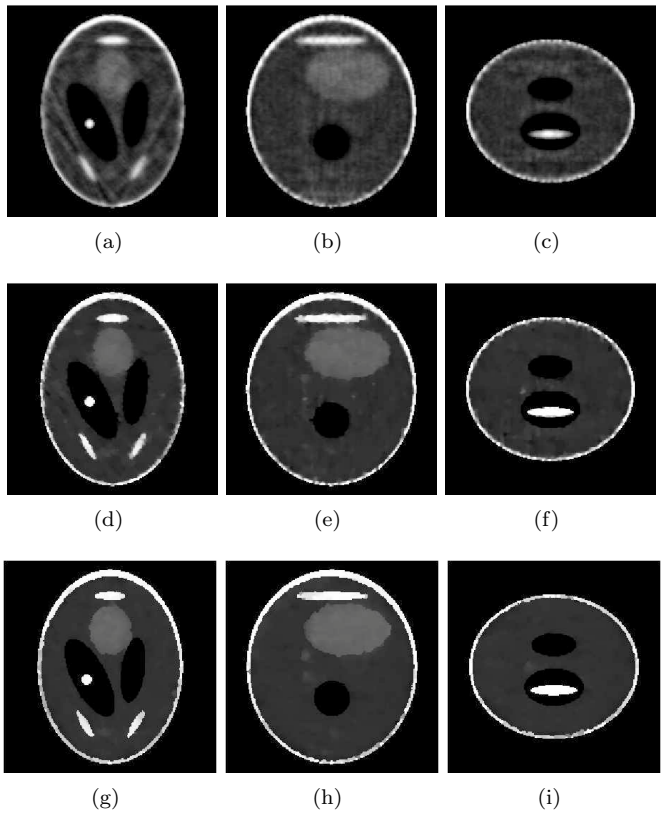

Figure 9. Reconstruction results with noisy projections, 2.0% Gaussian noise. The top to bottom and left to right rules are identical to those depicted figure 3. The RMSE ratios are 13.95%, 11.03%, and 7.22% for L2, L1 and L0 norm priors respectively.

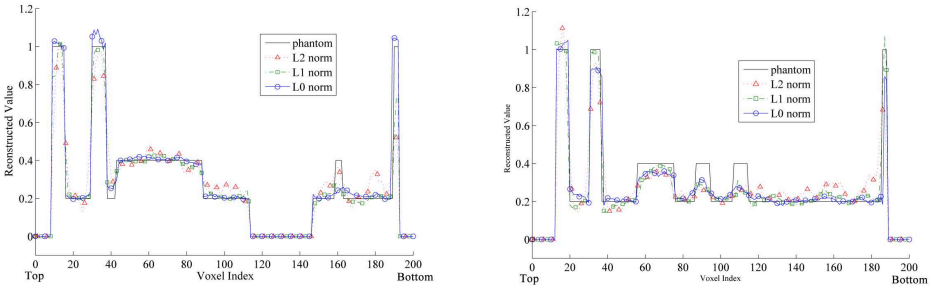

Figure 10. Line profile for noisy projections (2.0% additive Gaussian noise) reconstructions, corresponding to vertical line placed in Fig. 2 (a) and (b)

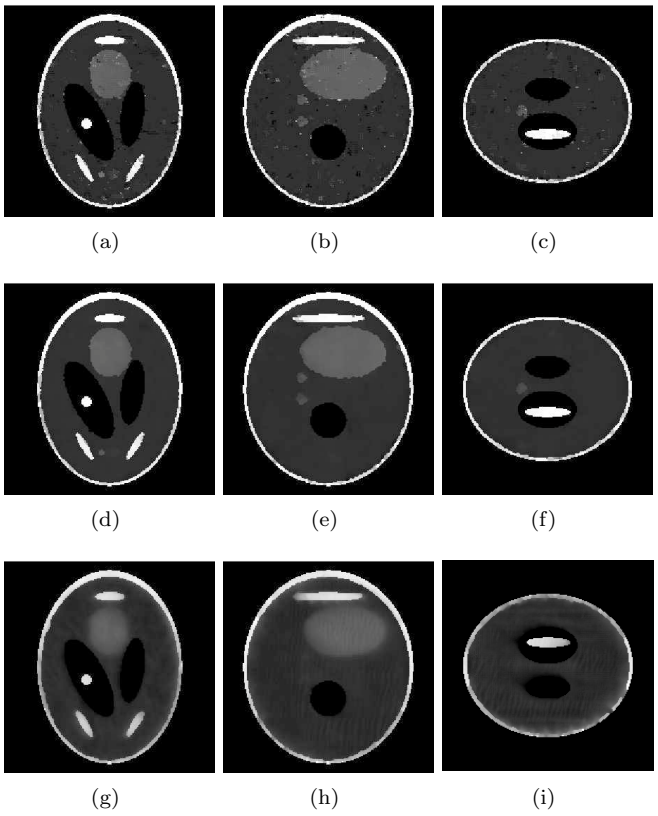

Figure 11. Rconstructions results with different relaxation parameter. From top to bottom are results with u_ρ =0.4, 0.65 and 0.85. From left to right are 2D slices at z = 0 mm, x = 0 mm, and y = -20.0 mm.

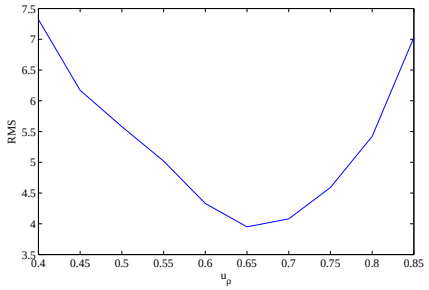

Figure 12. RMSE curve corresponding to different relaxation parameters.

also be considered (Johnson and Sofer; 1999; Sauer et al.; 1995; Zheng et al.; 2000).

The choice of parameters is another problem which deserves special attention. As we have seen, a key step for convergence in the proposed method is to iteratively approximate the "true L0-norm prior". In this paper, we have chosen a simple solution by introducing a relaxation parameter. We have shown that there is an optimal value for this relaxation parameter but additional experiments pointed out that any change in the phantom image, the noise level, or the number of projections leads to different curves with similar shapes. The valid lower bound for ρ rapidly increases with noise level in projections, so that it may be difficult to get satisfying reconstructions for high noise values. An effective noise suppression should be carried out before reconstruction.

6. Conclusion

Statistical iterative methods are often used to improve tomographic reconstructions using appropriate priors. However, the conventional MAP using MRF prior model can not provide satisfactory reconstructions from highly sparse sampled projections. In the present work, an iterative reconstruction method using L0-norm prior has been designed for multislice helical CT. This is equivalent to the L0-norm minimization under sparse signals, a well known highly ill-posed problem. Since the solution is difficult to achieve directly, a set of surrogate functions has been considered to approximate the L0-norm. Compared to the L2-norm and L1-norm priors, the L0-norm one is able to provide better reconstructions from few projections, while the quality of reconstructions with the former two priors is poor. To prevent the algorithm from falling into local minima, a progressive optimization scheme has been proposed. Although more iterations may be needed before the final solution is reached, the computational cost for projection and back-projection is rather small since the projection data is highly sparse sampled. With a carefully designed approximation scheme, the proposed method is still able to offer high quality reconstructions with noisy projection data. For the optimization of the method, we used a quadratic form objective function for the update of each pixel. This is similar to the well-known SPS algorithm but the difference is that the statistical model is assumed to be Gaussian, therefore there is no need to find a surrogate function for the likelihood function. This not only reduces the computation cost, but also accelerates the convergence speed. The proposed L0-SPS methods provides an effective way for reconstruction from highly sparse projections, which is helpful in low-dose CT scan. Computation time cost, noise control and choice of parameters are the three main issues currently examined.

Acknowledgements

The authors thank Dr. Jean-Louis Coatrieux for his contributions in conducting this work. They are also indebted to Dr. Jian Zhou for his discussion. This project has been supported by the National Basic Research Program of China (N°2010CB732503).

References

Becker, C., Knez, A., Leber, A., Treede, H., Ohnesorge, B., Schoepf, U. and Reiser, M. (2002). Detection of coronary artery stenoses with multislice helical CT

angiography, *Journal of computer assisted tomography* **26**(5): 750.

Candès, E., Braun, N. and Wakin, M. (2007). Sparse signal and image recovery from compressive samples, *4th IEEE International Symposium on Biomedical Imaging: From Nano to Macro, 2007. ISBI 2007*, pp. 976–979.

Candès, E. and Romberg, J. (2005). Practical signal recovery from random projections, *IEEE Trans. Signal Processing* .

Chartrand, R. (2007). Exact reconstruction of sparse signals via nonconvex minimization, *IEEE Signal Processing Letters* **14**(10): 707.

Donoho, D. (2006). For most large underdetermined systems of linear equations the minimal 𝓁 1-norm solution is also the sparsest solution, *Communications on pure and applied mathematics* **59**(6): 797–829.

Erdogan, H. and Fessler, J. (1999a). Monotonic algorithms for transmission tomography, *IEEE Transactions on Medical Imaging* **18**(9): 801–814.

Erdogan, H. and Fessler, J. (1999b). Ordered subsets algorithms for transmission tomography, *Physics in Medicine and Biology* **44**: 2835–2851.

Fessler, J. and Erdogan, H. (1998). A paraboloidal surrogates algorithm for convergent penalized-likelihood emission image reconstruction, *Proc. IEEE Nuc. Sci. Symp. Med. Im. Conf*, Vol. 2, Citeseer, pp. 1132–5.

Fessler, J. and Hero, A. (1994). Space-alternating generalized expectation-maximization algorithm, *IEEE Transactions on Signal Processing* **42**(10): 2664–2677.

Fessler, J. and Hero, A. (1995). Penalized maximum-likelihood image reconstruction using space-alternating generalized EM algorithms, *IEEE Transactions on Image Processing* **4**(10): 1417–1429.

Hsieh, J. (1997). Nonstationary noise characteristics of the helical scan and its impact on image quality and artifacts, *Medical Physics* **24**: 1375.

Iatrou, M., De Man, B., Basu, S., Res, G. and Niskayuna, N. (2006). A comparison between Filtered Backprojection, Post-Smoothed Weighted Least Squares, and Penalized Weighted Least Squares for CT reconstruction, *IEEE Nuclear Science Symposium Conference Record, 2006*, Vol. 5.

Johnson, C. and Sofer, A. (1999). A data-parallel algorithm for iterative tomographic image reconstruction, *Proc. of 7th IEEE Symp. Front Mass Parallel Computing*.

JUNG, K., LEE, K., KIM, S., KIM, T., PYEUN, Y. and LEE, J. (2000). Low-dose, volumetric helical CT: image quality, radiation dose, and usefulness for evaluation of bronchiectasis, *Investigative radiology* **35**(9): 557.

Knaup, M., Kalender, W. and Kachelrieß, M. (2006). Statistical cone–beam CT image reconstruction using the Cell broadband engine, *IEEE Medical Imaging Conference Record*, pp. 2837–2840.

La Rivière, P. (2005). Penalized-likelihood sinogram smoothing for low-dose CT, *Medical Physics* **32**: 1676.

Li, T., Li, X., Wang, J., Wen, J., Lu, H., Hsieh, J. and Liang, Z. (2004). Nonlinear sinogram smoothing for low-dose X-ray CT, *IEEE Transactions on Nuclear Science* **51**(5): 2505–2513.

Lu, H., Hsiao, T., Li, X. and Liang, Z. (2001). Noise properties of low-dose CT projections and noise treatment by scale transformations, *2001 IEEE Nuclear Science Symposium Conference Record*, Vol. 3.

Manglos, S., Gagne, G., Krol, A., Thomas, F. and Narayanaswamy, R. (1995). Transmission maximum-likelihood reconstruction with ordered subsets for cone beam CT, *Physics in Medicine and Biology* **40**: 1225–1241.

Naidich, D., Marshall, C., Gribbin, C., Arams, R. and McCauley, D. (1990). Low-dose CT of the lungs: preliminary observations, *Radiology* **175**(3): 729–731.

Nielsen, T., Manzke, R., Proksa, R. and Grass, M. (2005). Cardiac cone-beam CT volume reconstruction using ART, *Medical Physics* **32**: 851.

Nieman, K., Oudkerk, M., Rensing, B., van Ooijen, P., Munne, A., van Geuns, R. and de Feyter, P. (2001). Coronary angiography with multi-slice computed tomography, *The Lancet* **357**(9256): 599–603.

Pouliot, J., Bani-Hashemi, A., Chen, J., Svatos, M., Ghelmansarai, F., Mitschke, M., Aubin, M., Xia, P., Morin, O., Bucci, K. et al. (2005). Low-dose megavoltage cone-beam CT for radiation therapy, *International journal of radiation oncology, biology, physics* **61**(2): 552–560.

Rogers, L. (2002). Dose reduction in CT: how low can we go?, *American Journal of Roentgenology* **179**(2): 299.

Ropers, D., Baum, U., Pohle, K., Anders, K., Ulzheimer, S., Ohnesorge, B., Schlundt, C., Bautz, W., Daniel, W. and Achenbach, S. (2003). Detection of coronary artery stenoses with thin-slice multi-detector row spiral computed tomography and multiplanar reconstruction, *Circulation* **107**(5): 664.

Rusinek, H., Naidich, D., McGuinness, G., Leitman, B., McCauley, D., Krinsky, G., Clayton, K. and Cohen, H. (1998). Pulmonary nodule detection: low-dose versus conventional CT., *Radiology* **209**(1): 243.

Sauer, K., Borman, S. and Bouman, C. (1995). Parallel computation of sequential pixel updates in statistical tomographic reconstruction, *Proc. IEEE Intl. Conf. on Image Processing*, Vol. 3, pp. 93–6.

Sidky, E. and Pan, X. (2008). Image reconstruction by constrained, total-variation minimization, *Physics in medicine and biology* **53**: 4777–4807.

Slovis, T. (2002). CT and computed radiography: the pictures are great, but is the radiation dose greater than required?, *American Journal of Roentgenology* **179**(1): 39.

Sukovic, P. and Clinthorne, N. (2000). Penalized weighted least-squares image reconstruction for dual energy X-ray transmission tomography, *IEEE transactions on medical imaging* **19**(11): 1075–1081.

Thibault, J., Sauer, K., Bouman, C. and Hsieh, J. (2003). High quality iterative image reconstruction for multi-slice helical CT, *International Conference on Fully 3D Reconstruction in Radiology and Nuclear Medicine, Saint Malo, France*, Citeseer.

Trzasko, J. and Manduca, A. (2009). Highly undersampled magnetic resonance image reconstruction via homotopic l0-minimization, *IEEE Trans. Medical Imaging* **28**(1): 106–121.

Wang, J., Li, T., Lu, H. and Liang, Z. (2006). Noise reduction for low-dose single-slice helical CT sinograms, *IEEE transactions on nuclear science* **53**(3): 1230.

Zheng, J., Saquib, S., Sauer, K., Bouman, C. et al. (2000). Parallelizable Bayesian tomography algorithms with rapid, guaranteed convergence, *IEEE Transactions on Image Processing* **9**(10): 1745–1759.

Zou, Y. and Pan, X. (2004). Image reconstruction on PI-lines by use of filtered backprojection in helical cone-beam CT, *Physics in Medicine and Biology* **49**: 2717–2731.